High-order multiplicity in high-mass star formation

Shanghuo Li[1*], Patricio Sanhueza[2,3], Henrik Beuther[1], Huei-Ru Vivien Chen[4], Rolf Kuiper[5], Fernando A. Olguin[4], Ralph E. Pudritz[6], Ian W. Stephens[7], Qizhou Zhang[8], Fumitaka Nakamura[2,3], Xing Lu[9], Rajika L. Kuruwita[10], Takeshi Sakai[11], Thomas Henning[1], Kotomi Taniguchi[2], and Fei Li[12]

[1]Max Planck Institute for Astronomy, Heidelberg, Germany; shanghuo.li@gmail.com
[2]National Astronomical Observatory of Japan, National Institutes of Natural Sciences, Tokyo, Japan
[3]Department of Astronomical Science, School of Physical Science, SOKENDAI (The Graduate University for Advanced Studies), Tokyo, Japan
[4]Institute of Astronomy and Department of Physics, National Tsing Hua University, Hsinchu, Taiwan
[5]Faculty of Physics, University of Duisburg-Essen, Duisburg, Germany
[6]Origins Institute and Department of Physics and Astronomy, McMaster University, Hamilton, Ontario, Canada
[7]Department of Earth, Environment, and Physics, Worcester State University, Worcester, MA, USA
[8]Center for Astrophysics, Harvard & Smithsonian, Cambridge, MA, USA
[9]Shanghai Astronomical Observatory, Chinese Academy of Sciences, Shanghai, People's Republic of China
[10]Heidelberg Institute for Theoretical Studies, Heidelberg, Germany
[11]Graduate School of Informatics and Engineering, The University of Electro-Communications, Tokyo, Japan
[12]School of Astronomy and Space Science, Nanjing University, People's Republic of China

The dominant mechanism forming multiple stellar systems in the high-mass regime ($M_* \gtrsim 8\ M_\odot$) remained unknown because direct imaging of multiple protostellar systems at early phases of high-mass star formation is very challenging[1–3]. High-mass stars are expected to form in clustered environments containing binaries and higher-order multiplicity systems[4,5]. So far only a few high-mass protobinary systems, and not higher-order multiples, have been detected[6–12]. Here we report the discovery of quintuple, quadruple, triple, and binary protostellar systems simultaneously forming in a single high-mass protocluster, G333.23–0.06, using ALMA high-resolution observations. This provides the most clear direct measurement of the initial configuration of primordial high-order multiple systems, with implications for the in situ multiplicity and its origin. We find that the binary and higher-order multiple systems, and their parent cores, show no obvious sign of disk-like kinematic structure. We conclude that the observed fragmentation into binary and higher-order multiple systems can be explained by core fragmentation[13], indicating its crucial role in establishing the multiplicity during high-mass star cluster formation.

High-mass stars in the Milky Way are overwhelmingly (>80%; refs.[3,14–16]) found in binaries or higher-order multiplicity systems that play a key role in governing cluster dynamics and stellar evolution[17,18]. However, it is yet unclear whether they are predominantly formed from

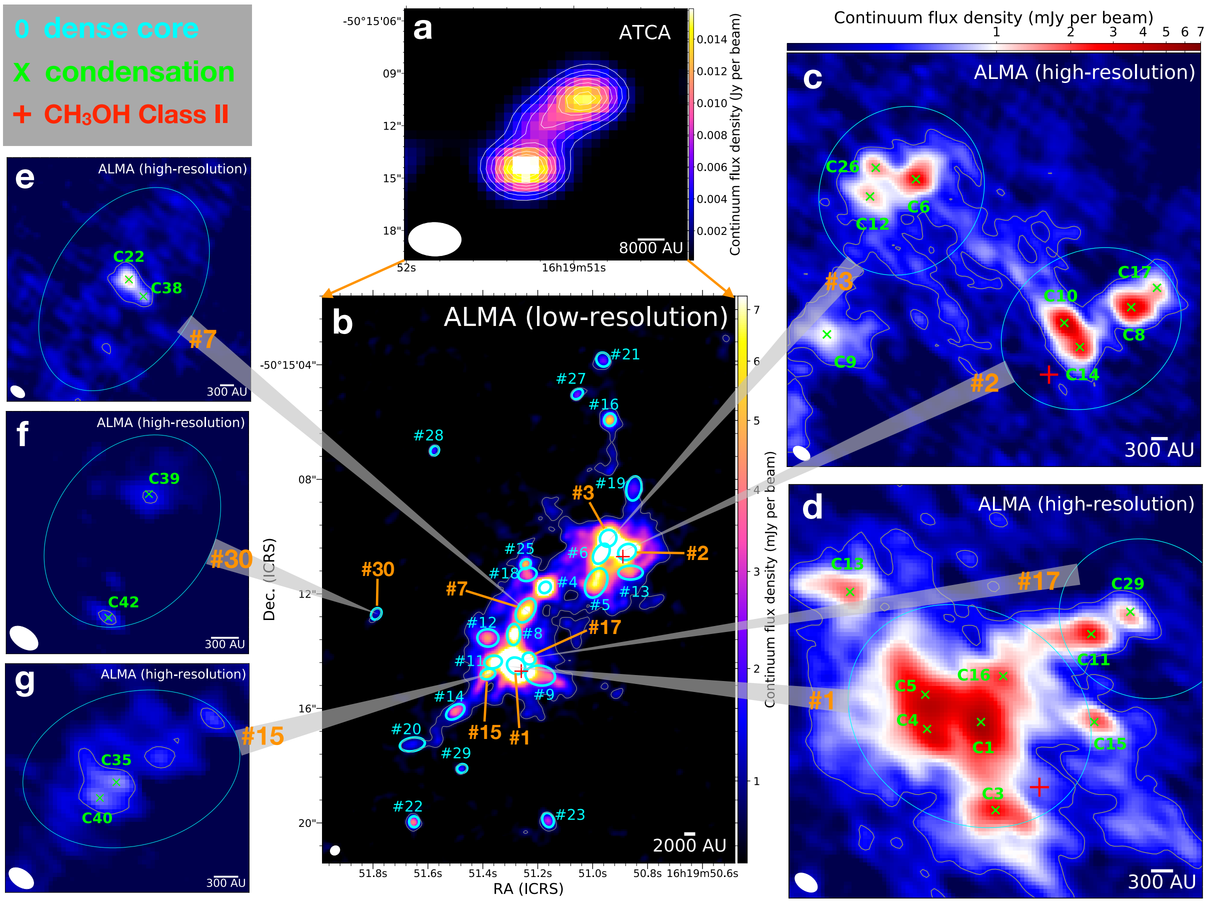

Fig. 1 | Continuum images of ATCA (3.3 mm), ALMA low-resolution (1.3 mm), and ALMA high-resolution (1.3 mm) observations. **a**, ATCA 3.3 mm continuum image ($\theta \sim 2.42''$). The contour levels are [5, 8, 11, 14,17, 20, 23, 26, 29] $\times\ \sigma$, where σ=0.6 mJy beam^{-1}. **b**, ALMA low-resolution ($\theta \sim 0.32''$) 1.3 mm continuum image. The contour is the 7 σ, where σ=0.16 mJy beam^{-1}. The ellipses show the identified cores based on the low-resolution continuum image. The red pluses are the Class II CH_3OH maser[23]. **c–g**, ALMA high-resolution ($\theta \sim 0.05''$) 1.3 mm continuum image for multiple systems. The green crosses present the identified condensations based on the ALMA high-resolution continuum image. The contour is the 7σ, where σ=0.05 mJy beam^{-1}. The dense cores (#1, #2, #3, ...) and condensations (C1, C2, C3, ...) are numbered in order of descending integrated intensity. Dense core #1 fragments into quintuple condensation system (C1, C3, C4, C5, C16), dense core #2 fragments into quadruple condensation system (C8, C10, C14, C17), dense core #3 fragments into triple condensation system (C6, C12, C26), and dense cores #7, #15, #17, and #30 fragment into binary condensation systems of C22-C38, C35-C40, C11-C29, and C39-C42, respectively. The white ellipses in the lower left corner of each panel denote the synthesized beam of continuum images.

in situ fragmentation at various scales (e.g., disks[19], cores[13], or filaments[20]) or subsequent stellar capture in clusters[21] because lacking direct measurements of their initial configuration and properties at the early phases of cluster formation.

We report the direct imaging of 1 quintuple, 1 quadruple, 1 triple, and 4 binary systems in the high-mass protocluster G333.23–0.06 (hereafter G333) by using Atacama Large Millimeter/submillimeter Array (ALMA) long-baseline observations (Fig. 1 and Methods). These binary and higher-order systems are detected in the high-resolution ($\theta \sim 0.05''$, equivalent to

260 au at the source distance of 5.2 kpc; ref.[22]) 1.3 mm dust continuum image. The detected condensations have radii between 153 and 678 au (Extended Data Table. 1). We refer to both binary and higher-order systems simply as multiple systems in what follows, and we only make an explicit distinction between the two when necessary.

The projected separations of these multiple systems are between 327 and 1406 au, with a mean value of 730 au, in good agreement with the typical projected separation of 700 au in the simulation of multiple star formation via core fragmentation[24]. The ambient gas masses ($M_{\rm amb}$) of these multiple systems range from 0.10 to 1.47 $M_\odot$ on the basis of the thermal dust emission (Methods). These masses are regarded as lower limits because the observations suffered from missing flux in the interferometer data. We focus primarily on the multiple systems that are embedded in a single dense core (typical radius of $\sim$2100 au; Fig. 1). The quintuple system consists of a small group of condensations (C1-C4-C5-C16), which is tightly connected as seen in dust continuum emission, and a condensation (C3) slightly separated. That is nevertheless part of the original parental core (Fig. 1). The quadruple system includes two binary configurations (C10-C14 and C8-C17), and the triple system composes three slightly separated condensations (C6, C12, and C26). The binary systems are C22-C38, C39-C42, and C35-C40.

In addition to the projected proximity on the sky of observed condensations, the line-of-sight velocity is another important diagnostic tool to determine whether members of a multiple system are physically associated. All members of each multiple system have similar centroid velocities (Methods), indicating that the members are physically associated and share a common origin.

Multiple systems formed via core fragmentation

The parent cores of the multiple systems are revealed in the lower-resolution ($\theta \sim 0.32''$, equivalent to 1664 au) 1.3 mm dust continuum image (Fig. 1). The dense cores are identified with radii ranging from 927 to 3443 au (Extended Data Table. 1). The multiple condensation systems are embedded in the dense cores. Each condensation likely harbors embedded protostellar object(s) as evidenced by the presence of hot ($T_{\rm gas}$ = 108–665 K) and warm ($E_u/k > 45$ K) gas resulting from internal heating (Methods), except for C39 and C42 where no significant molecular warm transitions (i.e., $E_u/k > 45$ K) are detected.

There is no obvious sign of a disk-like kinematic structure around any of the multiple systems and their parent cores in any of the lines we examined (Fig. 2 and Methods), including the typical disk tracers, e.g., CH_3CN, $^{13}CH_3CN$, and CH_3OCHO, and dense gas tracer, e.g., CH_3OH, $^{13}CH_3OH$, SO_2, SO, HC_3N, HNCO, NH_2CHO, H_2CO, and $H_2^{13}CO$. Meanwhile, the presence of the SiO outflows rules out the scenario of a weak velocity gradient resulted from projection of a face-on geometry (Fig. 2). In addition, the scenario in which multiple systems form by dynamical capture in a forming cluster, which have typical separations $>10^3$ au and significant different velocities[25], is inconsistent with the observed separation distributions and small velocity differences. These results demonstrate that the detected multiple systems are formed from core fragmentation, although disk fragmentation may still occur on smaller scales than those we can resolve with the current spatial resolution. The measured separations of the multiple systems (a mean value of 730 au) are smaller than the expected Jeans lengths of 5000–10000 au for thermal Jeans fragmentation of the parent cores of the multiple systems. The temperatures and volume densities of the parent cores used in Jeans analysis are T = 80–340 K and $n_{\rm H2} = 3 \times 10^6$–$1 \times 10^7$ cm^{-3}, respectively. The estimated Jeans lengths are conservative upper limits to the separations of fragments since the derived volume densities of parental cores are lower limits due to the missing flux. The turbulent Jeans fragmentation yields even larger separation than that of the thermal one because the non-thermal velocity dispersion is

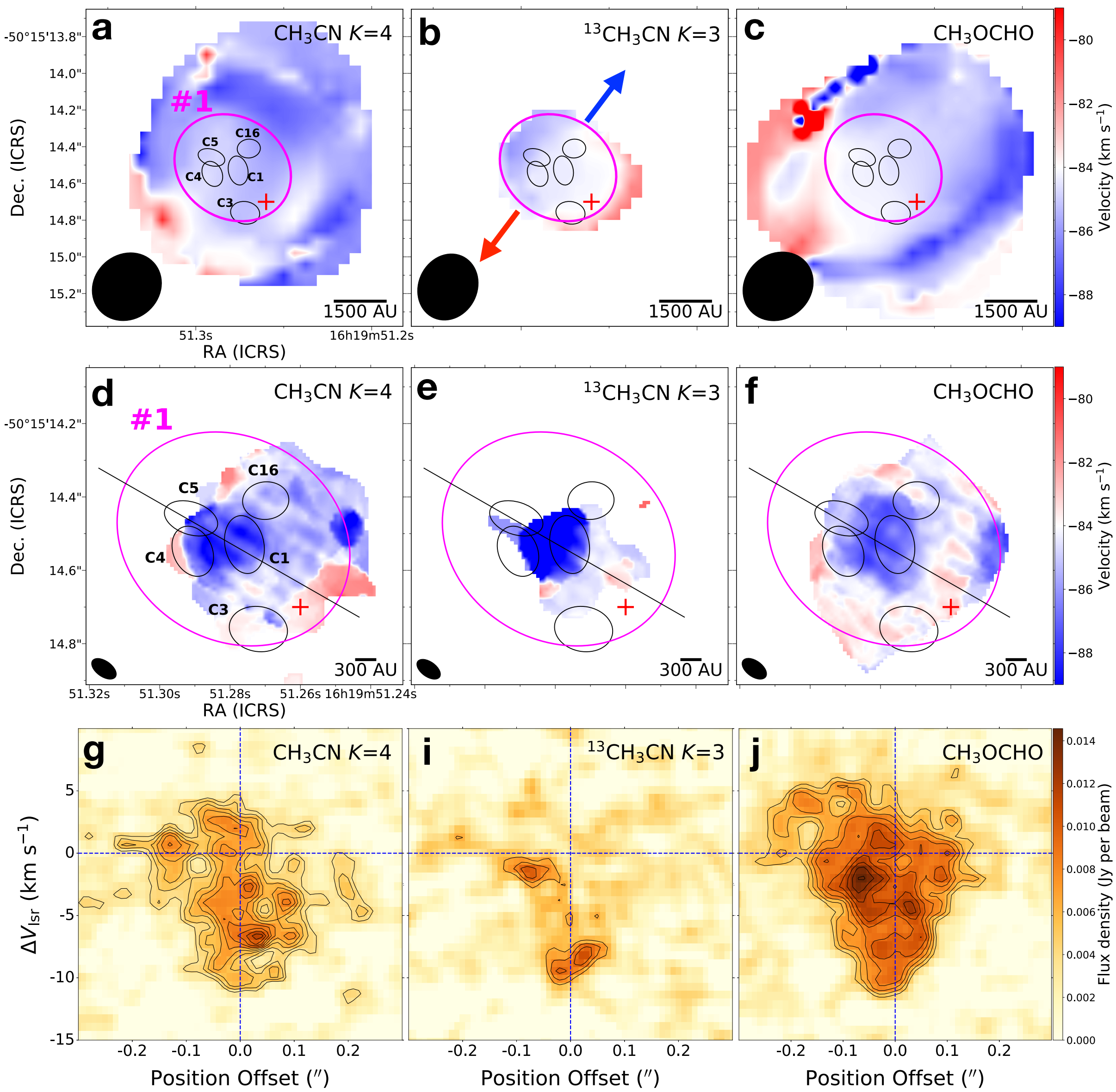

Fig. 2 | Examples of intensity-weighted velocity maps and position-velocity (PV) diagrams of CH_3CN $12_4 - 11_4$ (left column), $^{13}CH_3CN$ $12_3 - 11_3$ (middle column), and CH_3OCHO $20_{0,20} - 19_{0,19}$ (right column) for the quintuple system. a–c, We show the intensity-weighted velocity maps derived from the ALMA low-resolution data. **d–f**, We present the intensity-weighted velocity maps derived from the ALMA high-resolution data. The black and magenta ellipses show the condensations and their parent cores, respectively. The red plus marks the Class II CH_3OH position. The blue and red arrows show the directions of the outflow seen in the SiO emission from the ALMA low-resolution data. The black ellipses in the lower left corner of each panel denote the synthesized beam of continuum images. The remaining velocity maps are presented in Extended Data Figs. 1–3. **g–j**, We show the PV diagram maps derived from the high-resolution data. Contours levels start at $4\sigma_{rms}$ and increase in step of $1\sigma_{rms}$ interval, where σ_{rms} is 1.2 mJy beam^{-1}. The cut lines of the PV diagram are indicated in **d–f** with black lines. The blue dashed lines in the vertical and horizontal directions show the position of the dense core #1 and its systemic velocity of V_{lsr} = -85 km s^{-1}.

higher than the thermal velocity dispersion. The discrepancy indicates that the core fragmentation, which facilitates the formation of multiple system, is not merely regulated by the thermal pressure and/or turbulence, but additional mechanisms might also be important. For instance, ongoing global collapse and dynamical interactions of multiple systems could lead to inward migration[26], which moves the fragments closer together.

Masses of the central protostars

Conventionally, the mass (M_*) of the central protostar can be estimated through modelling the rotation in a Keplerian disk. However, the estimation of dynamical masses of the central protostars is prevented by the non-detection of disk kinematic structures toward the multiple protostellar systems. On the other hand, M_* can be estimated from the bolometric luminosity and a zero-age main sequence (ZAMS) assumption for the young protostars, which could provide a mass comparable to the dynamical mass obtained from Keplerian rotation[27]. The luminosities of the central protostars, as estimated from the temperature profile, are between 30 and 4.4×10^4 $L_\odot$, corresponding to A0 to B0 spectral type ZAMS stars[28] (Methods). The masses are estimated to be between 2.2 and 17.1 $M_\odot$ according to the mass-luminosity (M-L) relation[29] (Extended Data Table 1). Three binary systems (C22-C38, C39-C42, C34-C40) do not have temperature measurements due to nondetection of CH_3CN and its isotopologues. There are 4 condensations (C1, C4, C10, C14) with a luminosity $\gtrsim 7\times10^3$ $L_\odot$, corresponding to a mass of $\gtrsim 9$ $M_\odot$. This shows that indeed high-mass protostars exist in the quintuple and quadruple systems, which is consistent with the presence of Class II CH_3OH maser emission toward these regions (Fig. 1). The results indicate that high- and low-mass multiple protostellar systems are simultaneously forming within G333.

Stability of the multiple systems

To determine whether a multiple system is bound, we used the ambient mass $M_{\rm amb}$ to compute the kinetic (E_i) and gravitational (W_i) energies for each member of the multiple systems (Methods). The derived E_i is smaller than $|W_i|$ for all condensations (Fig. 3 and Extended Data Fig. 4), suggesting that these multiple systems are gravitationally bound, except for two condensations (C10 and C14). If including the central protostellar masses, the multiple systems would be even more gravitationally bound because the gravitational energy will be even higher. Indeed, the E_i and W_i computed from protostellar mass M_* show that the $E_i/|W_i|$ ratio is below 0.1 and much smaller than those derived from the ambient mass (Extended Data Fig. 4). In addition, the $E_i/|W_i|$ ratio will be even smaller when both $M_{\rm amb}$ and M_* are included. Therefore, the multiple systems are gravitationally bound at the present stage. With 20 identified multiple systems in G333, the observed multiplicity fraction is MF = 20/44 $\approx$ 45%, which is the fraction of systems that are multiples (binary, triple, etc.), and companion frequency is CF = 46/44 $\approx$ 1.0, which is the average number of companions per system. The derived MF and CF are higher than those measured in Orion and Perseus star-forming regions for a similar separation range of 300–1400 au[30], indicating that the multiplicity could be higher in denser cluster-forming environments. The estimated MF and CF are regarded as lower limits because further fragmentation might occur at smaller scales than what we can resolve with the current observations, and low-mass objects could be missed due to the limited sensitivity. The results indicate that the multiplicity in clusters is established in the protostellar phase.

Perspectives

The discovery of these quintuple, quadruple, triple, and binary protostellar systems is the best observational evidence to show the imprints of core fragmentation in building multiplicity in high-mass cluster-forming environments. Although we cannot test if disk fragmentation is more important at smaller scales than what we have observed so far, we expect that more systems similar to G333 will be discovered given the high resolutions and high sensitivities

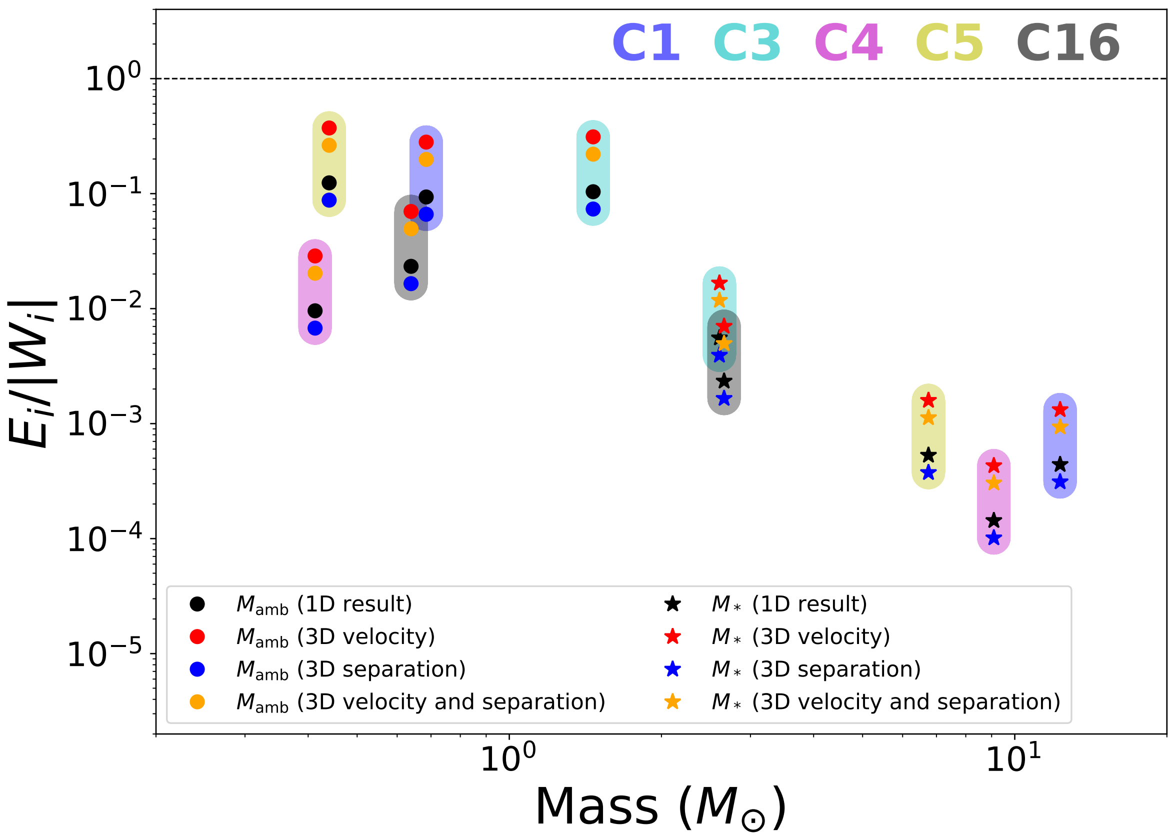

Fig. 3 | The kinetic-to-gravitational energy ratio $E_i/|W_i|$ as a function of mass for the quintuple system. The multiple systems with kinetic-to-gravitational energy ratio below unity are considered to be gravitationally bound. The circles and stars symbols are the results derived from ambient mass ($M_{\rm amb}$) and protostellar mass (M_*), respectively. $E_i/|W_i|$ has been estimated with four different methods: (1) line-of-sight velocity difference and on-sky separation (refer to one-dimensional, 1D; black symbols), (2) three-dimensional (3D) velocity difference ($\sqrt{3}$ times the line-of-sight velocity difference) and on-sky separation (red symbols), (3) line-of-sight velocity difference and 3D separation ($\sqrt{2}$ times the on-sky separation, blue symbols), (3) 3D velocity difference and 3D separation (orange symbols). The black dashed line marks $E_i/|W_i| = 1$. The condensations are marked with different color shadows, i.e., C1 (blue), C3 (cyan), C4 (red), C5 (yellow), and C16 (black). The remaining condensations are shown in Extended Data Fig. 4.

of ALMA observations. The statistics of these systems will help to benchmark the relative contribution of core fragmentation to the population of multiple stars in high-mass star clusters. Their properties will determine the initial conditions of multiple system formation, as well as the dynamical evolution in a cluster environment.

Methods

High-mass star-forming region G333.23–0.06

G333.23–0.06 is a high-mass star-forming region[31–34] at a distance of 5.2 kpc[22] associated with Class II CH_3OH maser emission[23], which can only be excited in high-density regions by strong radiation fields, making it exclusively found in high-mass star-forming regions[35,36].

Observations and data reduction

Observations of G333 were performed with ALMA in Band 6 (at the wavelength of 1.3 mm) with the 12-m array using 41 antennas in configuration similar to C40-5 (hereafter short-baseline or low-resolution) on November-05-2016 and 42 antennas in configuration similar to C43-8 (hereafter long-baseline) on July-28-2019 (Project ID: 2016.1.01036.S; PI: Sanhueza). Observations were obtained as part of the Digging into the Interior of Hot Cores with ALMA (DIHCA) project[12,37,38]. The baseline lengths are 18.6–1100 m and 91–8547 m for short-baseline and long-baseline observations, respectively. The correlators were tuned to cover four spectral windows with a spectral resolution of 976.6 KHz ($\sim$1.3 km s^{-1}) and a bandwidth of 1.875 GHz. These windows covered the frequency ranges of 233.5–235.5 GHz, 231.0–233.0 GHz, 219.0–221.0 GHz, and 216.9–218.7 GHz. The quasar J1427–4206 was used for flux and bandpass calibration, and J1603–4904 for phase calibration. The total on-source time toward the G333 is 6 minutes for short-baseline observations and 19.6 minutes for long-baseline observations. The phase center used is (α(ICRS), δ(ICRS)) = 16h19m51.20s, $-50^\circ 15' 13.''00$.

The visibility data calibration was performed using the CASA (version 5.4.0-70) software package[39]. We produced continuum data from line-free channels and continuum-subtracted data cubes for each observation epoch using the procedure described in ref.[37]. We performed phase only self-calibration using the continuum data and the self-calibration solutions were applied to data cubes. To recover the extended emission, we combined the short-baseline and long-baseline self-calibration data for both continuum and data cubes (hereafter combined or high-resolution data). We produced images for short-baseline and combined data sets, separately. We used the TCLEAN task with Briggs weighting and a robust parameter of 0.5 to image the continuum. The resultant continuum images have a synthesized beam of $0.35'' \times 0.30''$ (1820 au$\times$1560 au, panel b of Fig. 1) with a position angle of P.A. = -46.18°, $0.059'' \times 0.038''$ (307 au$\times$198 au) with a P.A. = 56.23°, and $0.066'' \times 0.039''$ (343 au$\times$203 au, panels c–g of Fig. 1) with a P.A. = 54.47° for short-baseline, long-baseline and combined dataset, respectively. The achieved 1σ rms noise levels continuum images are about 0.16 mJy beam^{-1}, 0.05 mJy beam^{-1}, and 0.05 mJy beam^{-1} for short-baseline, long-baseline, and combined data, respectively. Data cubes for each spectral window were produced using the automatic masking procedure YCLEAN[40], which automatically cleans each map channel with custom-made masks. The lines images 1σ rms noise are about 10 mJy beam^{-1}, 3 mJy beam^{-1}, and 3 mJy beam^{-1} with a channel width of $\sim$0.65 km s^{-1} for short-baseline, long-baseline, and combined data, respectively. The largest recoverable angular scales are 3.5$''$ for short-baseline and combined data, as determined by the short-baselines in the array.

The Australia Telescope Compact Array (ATCA) 3.3 mm continuum image is retrieved from ref.[34] (panel a of Fig. 1). All images shown in this letter are prior to primary beam correction, while all measured fluxes have the primary beam correction applied.

Dense core and condensation identification

To describe the dense molecular structures, we follow the nomenclature in the literature in which cores refer to structures with sizes of $\sim 10^3 - 10^4$ au, and condensations refer to substructures within a core.

We use the astrodendro[1] algorithm and CASA-imfit task to extract dense cores from short-baseline 1.3 mm continuum image and condensations from the combined and long-baseline only 1.3 mm continuum images. The astrodendro identifies the changing topology of the surfaces as a function of contour levels and extracts a series of hierarchical structure over a range of spatial scales[41]. The performance of astrodendro in characterizing the dense structure parameters (e.g., size and position angle) is not always good, while CASA-imfit performs better in this regard via a two-dimensional Gaussian fit to the emission.

Therefore, we used astrodendro to pre-select dense structures (i.e., the leaves in the terminology of astrodendro) from the 1.3 mm continuum images. We then use the parameters of the pre-select structures from astrodendro as input to CASA-imfit for more accurate measurement of their parameters, including peak position, peak flux ($I_{\rm peak}$), integrated flux (S_ν), major and minor axise sizes (full width at half maximum; $\rm FWHM_{maj}$ and $\rm FWHM_{min}$), and position angle (PA).

The following parameters are used in computing the dendrogram: the minimum pixel value $min\_value = 5\sigma$, where σ is the rms noise of the continuum image; the minimum difference in the peak intensity between neighboring compact structures $min\_delta = 1\sigma$; the minimum number of pixels required for a structure to be considered an independent entity $min\_npix = N$, where N is the number of pixels in the synthesized beam area.

To remove suspicious condensations around the strong emission regimes caused by the diffuse emission in the combined data, we have performed a cross-comparison of condensation catalogue derived from the combined data with the condensations revealed by the long-baseline only data. We identified 30 dense cores in short-baseline 1.3 mm continuum image and 44 condensations in combined 1.3 mm continuum image. Extended Data Figs. 5 and 6 show the identified dense cores and condensations, respectively (see also Extended Data Table 1 for the properties of multiple systems).

Centroid velocity of condensation

The centroid velocity ($\rm V_{lsr}$) of each condensation is determined by fitting a CH_3OH $4_{2,2} - 3_{1,2}$ ($E_u/k = 45.46$ K) line that is detected in the majority of condensations in order to measure $\rm V_{lsr}$ in the same manner. The measured $\rm V_{lsr}$ have been validated by comparing with other dense gas tracers. We identify no clear velocity difference between the members of each multiple system (Extended Data Table 1), i.e., $\triangle \rm V_{lsr} < 1$ km s^{-1} that is smaller than the line-of-sight velocity differences (2.0–9.5 km s^{-1}) of the binary protostars in refs.[9,11], indicating that all members of each multiple system are associated with the same region.

Search for disk kinematic structure

The observations cover the typical disk tracers, including CH_3CN and its isotopologues, and CH_3OCHO, as well as other dense gas tracers, for instance H_2CO and its isotopologues, CH_3OH and its isotopologues, HC_3N, NH_2CHO, SO_2, SO, HNCO, HCOOH, ^{13}CS, and OCS. Using these molecular lines, we have searched for disk-like rotating structures for the multiple systems and their parent cores with both short-baseline and combined data which have a channel width of $\sim$0.65 km s^{-1}. The dense gas tracers are not sufficiently strong to allow a reliable determination of kinematic information for 3 binary systems (C39-C42, C35-C40, C32-C38) in the combined data.

There are no obvious sign of disk kinematic structures toward the parent cores of multiple systems in any of the lines we examined based on short-baseline and combined data (Fig. 2 and Extended Data Fig. 1). There are some lines with a velocity gradient in some dense cores, but no clear Keplerian disk-like rotating structure are found in the position-velocity (PV) diagram

[1]http://dendrograms.org/

toward these cores. The velocity gradients trace either the outflows, or the large scale gas motions (e.g., gas flow, toroidal motions[42]). These dense cores are associated with unipolar, bipolar, and/or perpendicular outflows identified by the SiO emission from the ALMA short-baseline data (Extended Data Fig. 1). The detailed analysis of molecular outflows is beyond the scope of this letter, and will be presented in a future paper.

We examined the multiple systems following the same routine but using the combined data, and similarly found signs of velocity gradient in some condensations, but no obvious rotational signatures of disks (Fig. 2 and Extended Data Fig. 2). Some velocity gradients are likely dominated by the outflows, while the others require higher angular resolution and sensitivity to spatially resolve the origin (e.g., unresolved outflows or accretion flows).

As shown in Extended Data Fig. 2, there is a redshifted velocity feature surrounding the blueshifted velocity toward C10 an C14. Two velocity components are detected toward C10 and C14. We have inspected these two velocity components separately, and found no obvious disk kinematic (Extended Data Fig. 3). Several mechanisms could lead to two velocity components toward C10 and C14, such as unresolved multiple sources, unresolved Keplerian disk, or unresolved protostellar feedback within the condensation. Higher spatial and spectral resolution observations are required to distinguish these possibilities and determine the origin of these multiple velocity components.

Estimate of gas temperatures

We derived the gas temperatures ($T_{\rm gas}$) using the K-ladder of CH_3CN $J = 12$–11 and $^{13}CH_3CN$ $J = 13$–12 transitions with the XCLASS package[43]. The Markov Chain Monte Carlo tasks built in XCLASS was used to explore the parameter space during the fitting process. For the combined data, the signal-to-noise ratios of the CH_3CN and $^{13}CH_3CN$ are not sufficient to derive a reliable temperature map in the majority of cores, and they are not detected in three binary systems (C22-C38, C39-C42, and C34-C40). To improve the signal-to-noise ratio with minimal nearby source(s) contamination, we averaged the spectra within a half beam size toward the condensations. We exclude the $K < 4$ ladders in regions where these lower energy transitions become optically thick, i.e., where line profile show self absorption or saturated emission. To improve the fitting of the CH_3CN and $^{13}CH_3CN$ lines, we include $CH_3^{13}CH$ $J = 12$–11 lines and other molecular lines (i.e., CH_3OH, HNCO) in fitting for CH_3CN and CH_3OCH_3 for $^{13}CH_3CN$, if they are detected. The derived rotational temperatures range from 108 to 665 K (Extended Data Table 1).

The rotational temperatures derived from $^{13}CH_3CN$ are higher than those of CH_3CN. This is because the CH_3CN lines have a higher optical depth and preferably trace the surface of the structure, while $^{13}CH_3CN$ is optically thinner and better trace the interior of the structure. This clearly suggests that these objects exhibit temperatures gradients and are internally heated by the protostar(s) at the centre. Therefore, we use the temperature derived from $^{13}CH_3CN$ to estimate the mass and luminosity, and in the case that $^{13}CH_3CN$ is not sufficiently strong to allow a temperatures measurement, we use the temperature derived from CH_3CN.

Computing the luminosity of the embedded protostar

With the derived gas temperature and taking into account the dust emissivity, we are able to approximately estimate the luminosity of the central heating source according to the relation between the temperature distribution and embedded protostellar luminosity[44,45], which is given by following equation

$$L = 10^5\, L_\odot \times \left[\left(\frac{T_D}{65\ \mathrm{K}}\right) \left(\frac{0.1}{f}\right)^{-1/(4+\beta)} \left(\frac{0.1\ \mathrm{pc}}{r}\right)^{-2/(4+\beta)} \right]^{4+\beta}, \tag{1}$$

where T_D is the dust temperature at the radius r, β is the power-law index of dust emissivity at far-infrared wavelengths and f is its value at the wavelength of 50 μm. The β usually ranges from 0 to 1[45]. The gas temperature derived from either $^{13}CH_3CN$ or CH_3CN based on the averaged spectrum within a half of beam size of the condensation's continuum peak can be used as a good approximation of T_D at the radius r = 130 au (corresponding to the half beam size of $\sim$0.025″), where the densities are sufficiently high ($> 10^{4.5}$ cm^{-3}) for the dust and gas to be well coupled[46]. The $^{13}CH_3CN$ and CH_3CN lines are not detected in 3 binary systems (C22–C38, C39–C42, C34–C40). Thus, we refrain from estimating the M_* for these condensations to avoid the large uncertainty.

Assuming $\beta = 0$, the derived luminosities range from 30 to 4.4×10^4 $L_\odot$ (Extended Data Table 1), corresponding to spectral A0- to B0-type ZAMS stars[28], whose mass would be about 2.2 to 17.1 $M_\odot$ according to the mass-luminosity (M-L) relation[29]. The total derived luminosities ($\sim$$9\times10^4$ $L_\odot$) appear to be comparable to the value ($\sim$$2\times10^4$ $L_\odot$) estimated in clump scale considering the uncertainties could up to a factor of a few[47]. There are 4 condensations (C1, C4, C10, and C14) with estimated luminosities of 7.1×10^3 – 4.4×10^4 $L_\odot$, corresponding to a B1–B0 spectral type ZAMS star of >9 $M_\odot$ (Extended Data Table 1). Therefore, a massive protostar should exist in these condensations, as also suggested by the presence of Class II CH_3OH maser, which are excited in high-density regions by strong radiation fields and exclusively tracing high-mass star-forming regions (Fig. 1). The derived luminosity will be even higher if a larger β is adopted.

Estimating ambient gas mass from dust continuum emission

The brightness temperatures of the dust emission in the condensations are lower than the gas temperatures $T_{\rm gas}$ which is a good approximation of T_D. To check if the dust emission is optically thin, we computed the optical depth $\tau_{\rm cont}$ of the continuum emission at the peak position of each condensation using[48]

$$\tau_\nu^{\rm beam} = -\ln\left(1 - \frac{S_\nu^{\rm beam}}{\Omega_{\rm A} B_\nu(T_D)}\right) \tag{2}$$

where B_ν is the Planck function at the dust temperature T_D, $S_\nu^{\rm beam}$ is the continuum peak flux density, $\Omega_{\rm A}$ is the beam solid angle. The condensations are dense enough (>$10^{4.5}$ cm^{-3}) for gas and dust to be well coupled and in thermal equilibrium. As such, the gas temperature derived from the $^{13}CH_3CN$ or CH_3CN should be approximately equal to the dust temperature. The derived mean optical depths are 0.03–0.27 with a mean value of 0.1 for all available condensations, indicating optically thin dust emission.

The observed 1.3 mm continuum emission is dominated by thermal dust emission toward G333 because the hydrogen recombination line (i.e., H30α) is not detected toward condensations and the ATCA 3.3 mm continuum emission is also dominated by dust emission[34]. We calculate the ambient gas mass for the condensations following

$$M_{\rm amb} = \eta \frac{S_\nu {\rm D}^2}{\kappa_\nu B_\nu(T_D)}, \tag{3}$$

where η = 100 is the gas-to-dust ratio, S_ν is the measured integrated source flux, $m_{\rm H}$ is the mass of an hydrogen atom, μ = 2.8 is the mean molecular weight of the interstellar medium, D = 5.2 kpc is the distance to the source, and κ_ν is the dust opacity at a frequency of ν. We adopted a value of 0.9 cm^{-2} g^{-1} for $\kappa_{1.3\rm mm}$, which corresponds to the opacity of thin ice mantles and a gas density of 10^6 cm^{-3} (ref.[49]). We use the lowest temperature of 108 K derived from CH_3CN as an approximation to the temperature for the condensations in which $^{13}CH_3CN$ and CH_3CN

are not detected. The actual temperature should be lower than 108 K, indicating that the derived mass is the lower limit for the condensations. The derived ambient gas masses are between 0.10 and 1.47 $M_\odot$ (Extended Data Table 1), with the mean and median values of 0.56 and 0.43 $M_\odot$, respectively. The estimated ambient gas masses should be regarded as lower limits due to the interferometric observations suffering from missing flux.

Stability analysis of multiple system

To assess the stability of the multiple system, we compute the potential and kinetic energy of each object following the approach introduced in ref.[20]. The gravitational potential energy, W_i, and kinetic energy, E_i, can be caculated by

$$W_i = -\sum_{i \neq j} \frac{G m_i m_j}{r_{ij}}, \tag{4}$$

$$E_i = \frac{1}{2} m_i (\mathrm{V_i} - \mathrm{V_{com}})^2, \tag{5}$$

where m_i and m_j are the masses of object i and j, r_{ij} is the separation between i and j, V_i is the (line-of-sight) velocity of object i, and $\mathrm{V_{com}}$ is the velocity of the centre of mass of the system. We determine the $\mathrm{V_{com}}$ through

$$\mathrm{V_{com}} = \frac{\sum\limits_k m_k V_k}{\sum\limits_k m_k}, \tag{6}$$

where m_k and V_k are the mass and velocity of the object k in the multiple system. A star with $E_i/|W_i| < 1$ is considered to be bound to the system.

The full velocity difference is $\sqrt{3}$ times the velocity difference along the line-of-sight, $\triangle \mathrm{V_{3D}} = \sqrt{3} \triangle \mathrm{V_{1D}} = \sqrt{3}(\mathrm{V_i} - \mathrm{V_{com}})$, assuming the measured velocity difference is representative of the one-dimensional velocity difference. Similarly, the total separation is $\sqrt{2}$ times the projected separation on the sky, $r_{3D} = \sqrt{2} r_{1D} = \sqrt{2} r_{ij}$, assuming that the measured projected separation is a good approximation of the separation along the line-of-sight. The observed mean separation, $\langle r_{1D} \rangle$, is about 730 au, which is consistent with the typical projected value of 700 au, $r_{1D} = r_{3D}/\sqrt{2} = 1000/\sqrt{2} = 700$ au, in the simulation of multiple star formation via core fragmentation[24].

We used the ambient mass M_{amb} and protostar mass M_* to calculate the kinetic and gravitational energies for condensations in both one- and three-dimensional scenarios. We find that all multiple systems are gravitationally bound (see Fig. 3 and Extended Data Fig. 4), with exceptions for two condensations (C10 and C14) that have $E_i/|W_i| > 1$ for 3D velocity difference in the case of using M_{amb}. However, these two condensations are gravitationally bound if the central protostar mass is considered. (see Extended Data Fig. 4). If the total mass, $M_{tot} = M_{amb} + M_*$, is used, the $E_i/|W_i|$ ratio will be smaller. Therefore, we conclude that all multiple systems are consistent with being gravitationally bound at the present stage. Extended Data Table 1 presents the E_i, and W_i for each condensation.

Data availability

This paper makes use of the following ALMA data: ADS/JAO.ALMA#2016.1.01036.S. The data are available at `https://almascience.nao.ac.jp/aq` by setting the observation code. The reduced data used for this study are available from the corresponding authors upon reasonable request.

Code availability

The ALMA data were reduced using CASA versions 5.4.0-70 that are available at https://casa.nrao.edu/casa_obtaining.shtml.

Acknowledgements

P.S. was partially supported by a Grant-in-Aid for Scientific Research (KAKENHI Number JP22H01271 and JP23H01221) of JSPS. R.K. acknowledges financial support via the Heisenberg Research Grant funded by the German Research Foundation (DFG) under grant no. KU 2849/9. R.E.P is supported by a Discovery grant from NSERC Canada. This work made use of the following ALMA data: ADS/JAO.ALMA#2016.1.01036.S. ALMA is a partnership of ESO (representing its member states), NSF (USA) and NINS (Japan), together with NRC (Canada), MOST and ASIAA (Taiwan), and KASI (Republic of Korea), in cooperation with the Republic of Chile. The Joint ALMA Observatory is operated by ESO, AUI/NRAO and NAOJ. Data analysis was in part carried out on the Multi-wavelength Data Analysis System operated by the Astronomy Data Center (ADC), National Astronomical Observatory of Japan.

Author contributions

S.L. wrote the main text, and led the data reduction and data analysis. P.S. led the ALMA proposal, and contributed to the interpretation of results and writing. H.B. assisted with the analysis and contributed to the interpretation of results. F.O. conducted the data calibration and commented on the article. All authors contributed to the discussed the results and implication, and commented on the article.

Competing interests

The authors declare no competing interests.

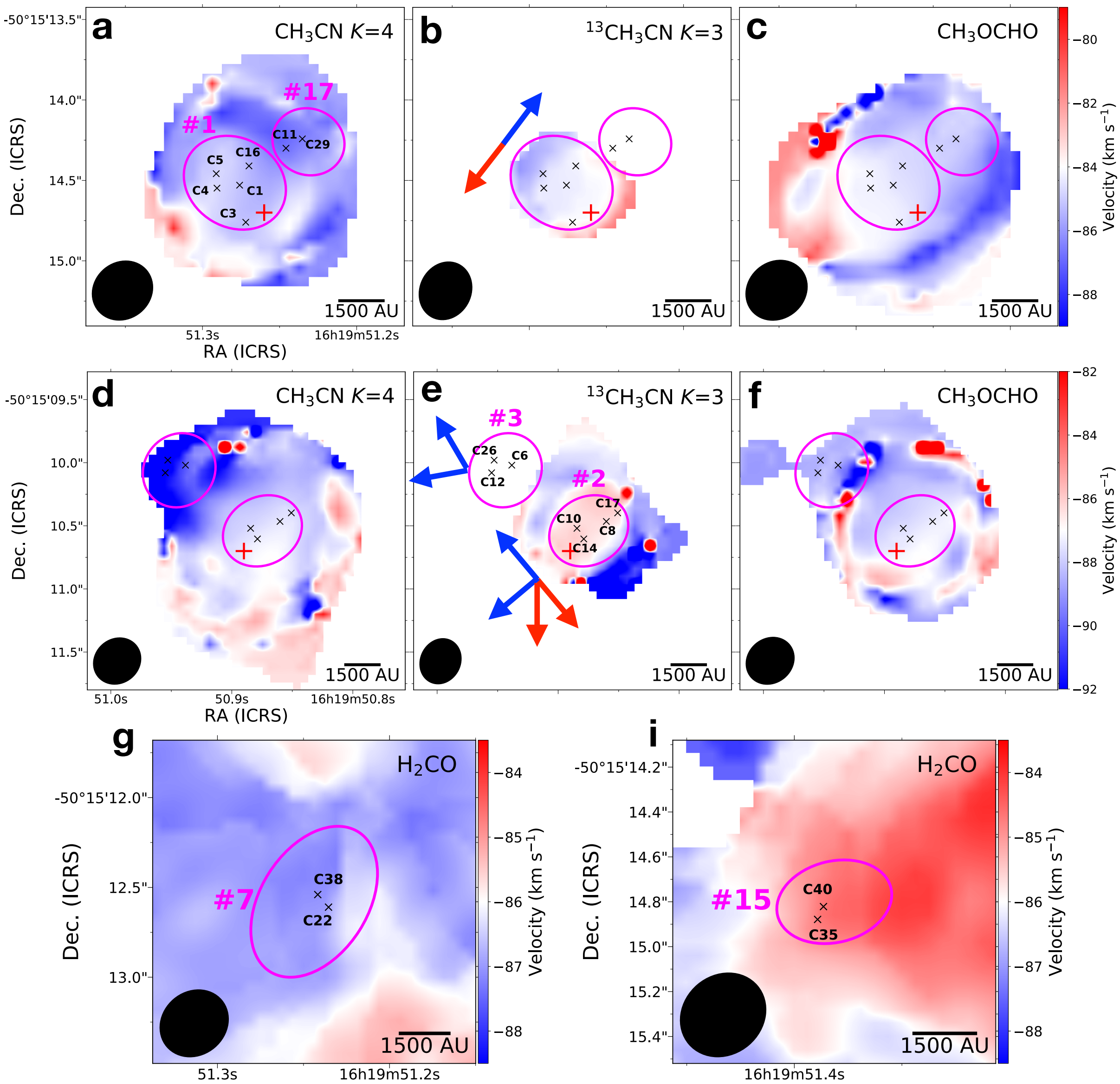

Extended Data Fig. 1 | Intensity-weighted velocity maps derived from the low-resolution data toward parent cores of multiple systems. **a–f**, We show intensity-weighted velocity maps of CH_3CN $12_4 - 11_4$ (**a** and **d**), $^{13}CH_3CN$ $12_3 - 11_3$ (**b** and **e**), and CH_3OCHO $20_{0,20} - 19_{0,19}$ (**c** and **f**) for dense cores #1, #17, #2, and #3. The blue and red arrows show the directions of the outflows seen in the SiO emission from the ALMA low-resolution data. **g–i**, Intensity-weighted velocity maps of H_2CO $3_{2,2} - 2_{2,1}$ for dense cores #7 (**g**) and #15 (**i**). The magenta ellipses and black crosses show the dense cores and their embedded condensations, respectively. The red plusses marks the Class II CH_3OH positions. The black ellipses in the lower left corner of each panel denote the synthesized beam of lines images.

Extended Data Table. 1 | Properties of condensations

Condensation	RA (hh:mm:ss.sss)	DEC (dd:mm:ss.sss)	I_{peak} (mJy beam^{-1})	S_ν (mJy)	size ($'' \times ''$, deg)	Radius ($''$[au])	V$_{lsr}$ (km s^{-1})	T_{gas} (K)	M_{amb} ($M_\odot$)	N_{H_2} (cm^{-2}) ($\times 10^{24}$)	$W_i(M_{amb})$ ($M_\odot$ km^{2}s^{-2}) ($\times 10^{-2}$)	$E_i(M_{amb})$ ($M_\odot$ km^{2}s^{-2}) ($\times 10^{-2}$)	L_{bol} ($L_\odot$)	M_* ($M_\odot$)	$W_i(M_*)$ ($M_\odot$ km^{2}s^{-2}) ($\times 10^{-2}$)	$E_i(M_*)$ ($M_\odot$ km^{2}s^{-2}) ($\times 10^{-2}$)
(1)	(2)	(3)	(4)	(5)	(6)	(7)	(8)	(9)	(10)	(11)	(12)	(13)	(14)	(15)	(16)	(17)
C1	16:19:51.275	-50:15:14.529	6.01	38.80±2.07	0.15×0.09, 5	0.12 [607]	-84.15±0.21	525±66	0.68	2.50	-138.03	12.91	16870	12.30	-287.17	12.65
C3	16:19:51.271	-50:15:14.760	2.58	19.21±0.94	0.15×0.11, 87	0.13 [671]	-84.76±0.09	126±1	1.47	4.64	-132.44	13.75	55	2.60	-49.83	27.69
C4	16:19:51.290	-50:15:14.548	3.27	18.79±2.00	0.13×0.09, 17	0.11 [572]	-84.39±0.25	423±15	0.41	1.69	-87.91	0.84	7103	9.09	-282.61	4.05
C5	16:19:51.291	-50:15:14.458	3.01	15.24±1.82	0.14×0.08, 76	0.10 [532]	-84.11±0.28	323±14	0.44	2.05	-85.09	10.56	2414	6.75	-227.02	12.04
C16	16:19:51.269	-50:15:14.410	1.74	8.57±0.65	0.11×0.09, 110	0.10 [515]	-84.67±0.14	128±1	0.64	3.06	-101.27	2.36	60	2.66	-76.98	18.01
C6	16:19:50.938	-50:15:10.020	2.99	14.21±0.74	0.11×0.08, 141	0.09 [494]	-90.52±0.15	150±1	0.90	4.47	-82.34	13.37	113	3.12		
C12	16:19:50.955	-50:15:10.080	1.43	10.69±0.80	0.18×0.09, 48	0.13 [678]	-89.95±0.13		0.95	3.00	-93.45	9.15				
C26	16:19:50.952	-50:15:09.980	1.65	3.95±0.58	0.07×0.05, 30	0.06 [310]	-90.06±0.19	130±5	0.29	2.85	-54.46	0.91	64	2.70		
C10	16:19:50.884	-50:15:10.520	4.52	10.99±0.69	0.06×0.06, 62	0.06 [313]	-88.67±0.15	532±5	0.19	1.85	-8.71	3.46	17820	12.53	-454.54	13.01
C8	16:19:50.860	-50:15:10.465	3.48	13.12±0.46	0.10×0.07, 83	0.08 [438]	-88.05±0.12	333±2	0.37	2.29	-17.88	4.04	2751	6.98	-197.18	78.34
C14	16:19:50.878	-50:15:10.604	2.63	9.97±0.81	0.10×0.06, 131	0.08 [414]	-88.68±0.14	665±8	0.14	0.86	-7.36	2.61	43555	17.12	-492.49	19.59
C17	16:19:50.850	-50:15:10.397	1.45	6.37±0.48	0.11×0.08, 25	0.09 [484]	-88.27±0.09	203±2	0.30	1.59	-15.07	0.13	377	4.23	-107.48	14.04
C11	16:19:51.245	-50:15:14.300	2.67	10.84±0.87	0.13×0.05, 101	0.08 [427]	-86.11±0.17	108±2	0.97	5.61	-10.30	0.03	31	2.19	-18.34	1.37
C29	16:19:51.235	-50:15:14.241	1.33	3.06±0.52	0.09×0.04, 55	0.06 [300]	-85.95±0.19	276±2	0.10	1.07	-10.30	0.30	1285	5.76	-18.34	0.52
C22	16:19:51.241	-50:15:12.540	1.21	4.81±0.43	0.10×0.07, 144	0.08 [440]	-87.53±0.06		0.43	2.56	-7.47					
C38	16:19:51.235	-50:15:12.610	0.73	1.49±0.33	0.09×0.06, 18[1]	0.07 [364][1]	-87.57±0.09		0.13	1.54	-7.47	0.01				
C35	16:19:51.386	-50:15:14.821	0.65	2.34±0.15	0.13×0.05, 69	0.08 [417]	-85.04±0.12		0.21	1.38	-4.91	0.19				
C40	16:19:51.389	-50:15:14.878	0.61	1.37±0.12	0.10×0.03, 72	0.05 [269]	-85.25±0.13		0.12	1.28	-4.91	0.32				
C39	16:19:51.784	-50:15:12.623	0.44	1.43±0.09	0.09×0.06, 104	0.07 [387]			0.13	0.92	-0.37					
C42	16:19:51.793	-50:15:12.879	0.53	0.73±0.10	0.05×0.02, 69	0.03 [153]			0.06	1.12	-0.37					

Note: Columns (1)–(3) present the name, right ascension, and declination of condensations. The continuum peak intensity, flux density, beam-deconvolved size, beam-deconvolved radius, and centroid velocity are shown in columns (4)–(8). Column (9) is the gas temperature derived from $^{13}CH_3CN$ or CH_3CN. Column (10) and (11) are the ambient mass and the H_2 column density. The gravitation potential energy and kinetic energy derived from M_{amb} are shown in columns (12) and (13). The luminosity and corresponding mass of central protostar are presented in columns (14) and (15). Columns (16) and (17) shows the gravitation potential energy and kinetic energy derived from M_*.

[a1] This is beam-convolved size due to the condensation marginally resolved.

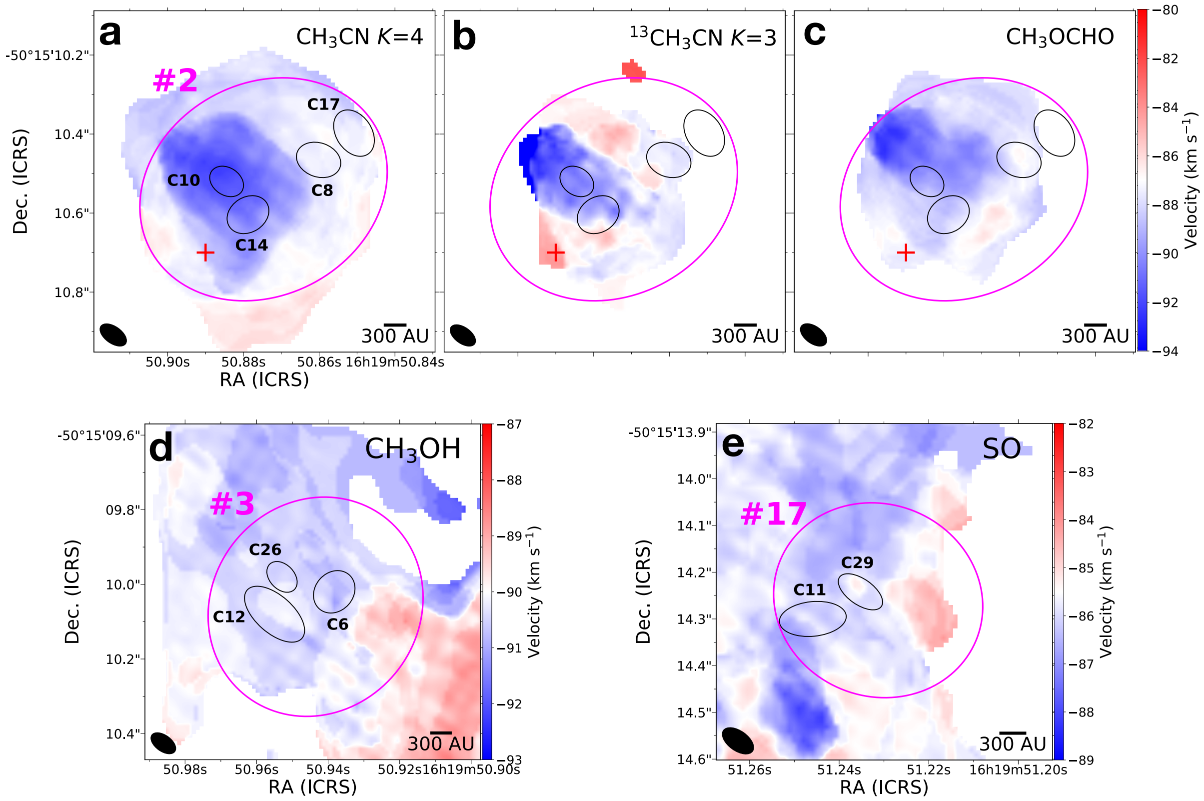

Extended Data Fig. 2 | Intensity-weighted velocity maps derived from the high-resolution data toward multiple systems. a–c, Intensity-weighted velocity maps of CH_3CN $12_4 - 11_4$ (**a**), $^{13}CH_3CN$ $12_3 - 11_3$ (**b**), and CH_3OCHO $20_{0,20} - 19_{0,19}$ (**c**) for the quadruple system. **d-e**, Intensity-weighted velocity maps of CH_3OH $4_{2,2} - 3_{1,2}$ (**d**) and SO $5,6 - 4,5$ (**e**) for the triple and the binary systems, respectively. The black and magenta ellipses show the condensations and their parent cores, respectively. The red plusses marks the Class II CH_3OH positions. The black ellipses in the lower left corner of each panel denote the synthesized beam of lines images.

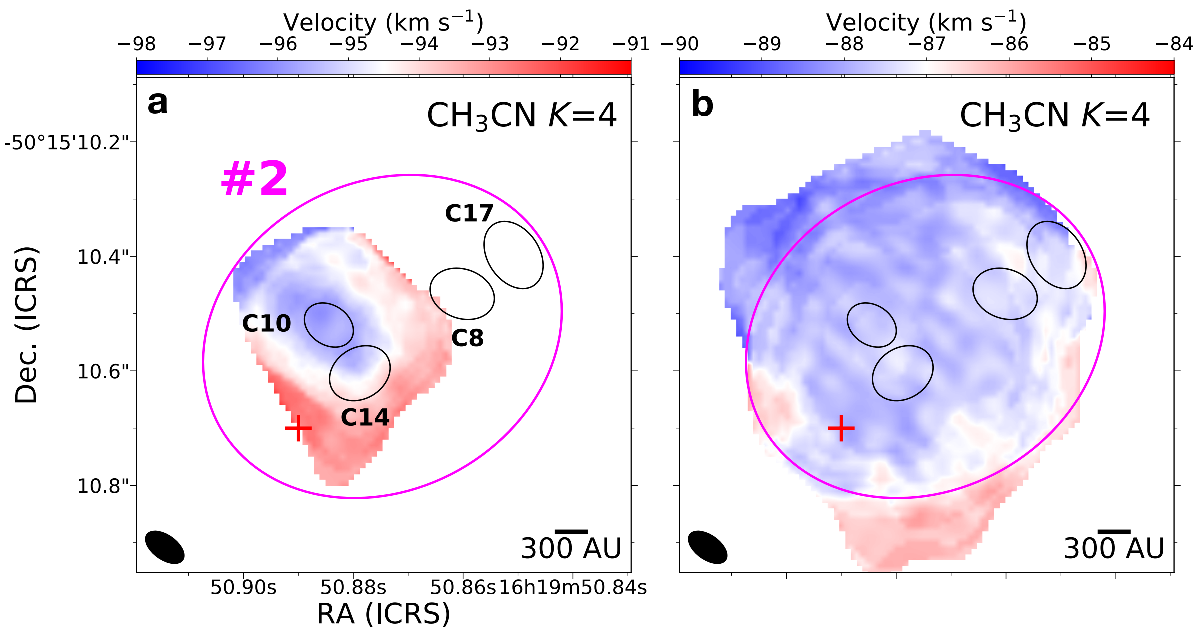

Extended Data Fig. 3 | Intensity-weighted velocity maps of CH_3CN $12_4 - 11_4$ for two velocity ranges of [-98, -91] km s^{-1} and [-90, -84] km s^{-1}. The black and magenta ellipses show the condensations and their parent cores, respectively. The red plusses marks the Class II CH_3OH positions. The black ellipses in the lower left corner of each panel denote the synthesized beam of lines images.

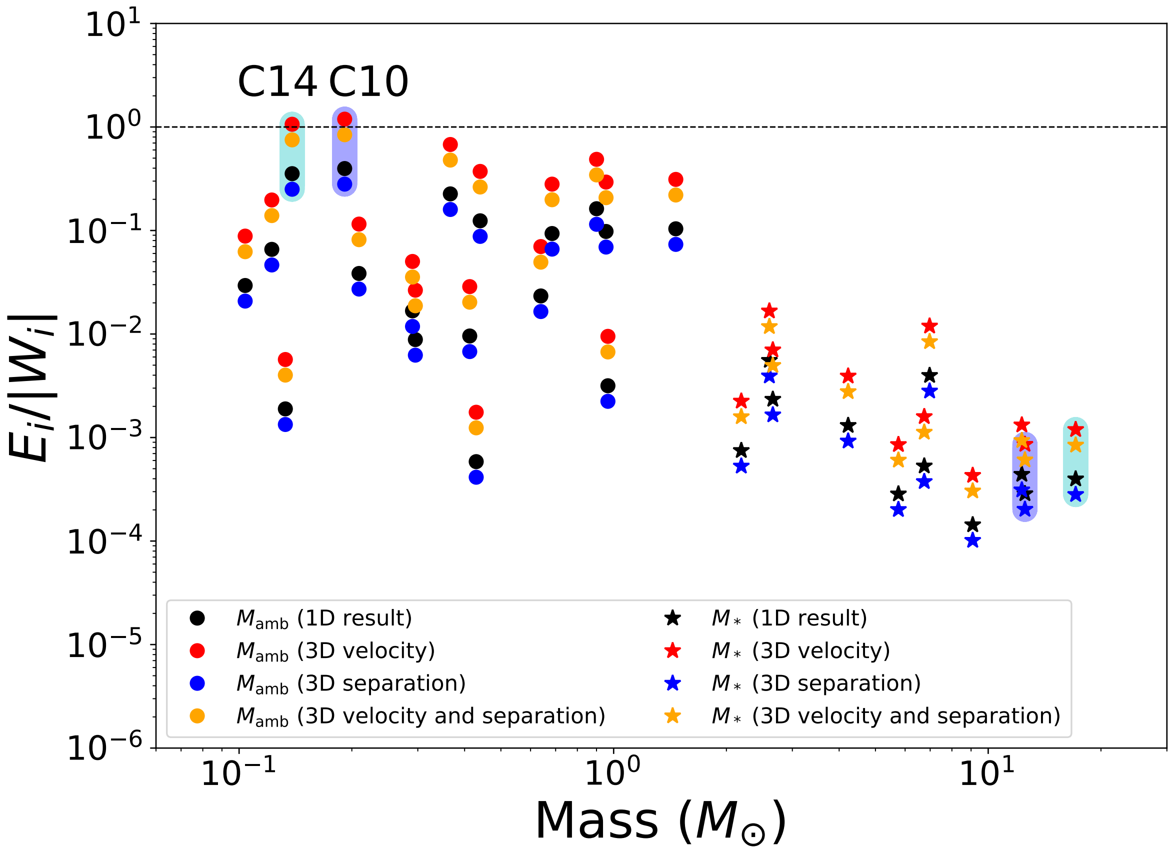

Extended Data Fig. 4 | Same as Fig. 3, but for all available condensations. There are two condensations (C10 and C14) with $E_i/|W_i| > 1$ for the 3D velocity scenario in the case of using $M_{\rm amb}$. If the central protostar mass is considered, the $E_i/|W_i|$ of these two condensations is smaller than 1. This figure indicates that all multiple systems are gravitationally bound.

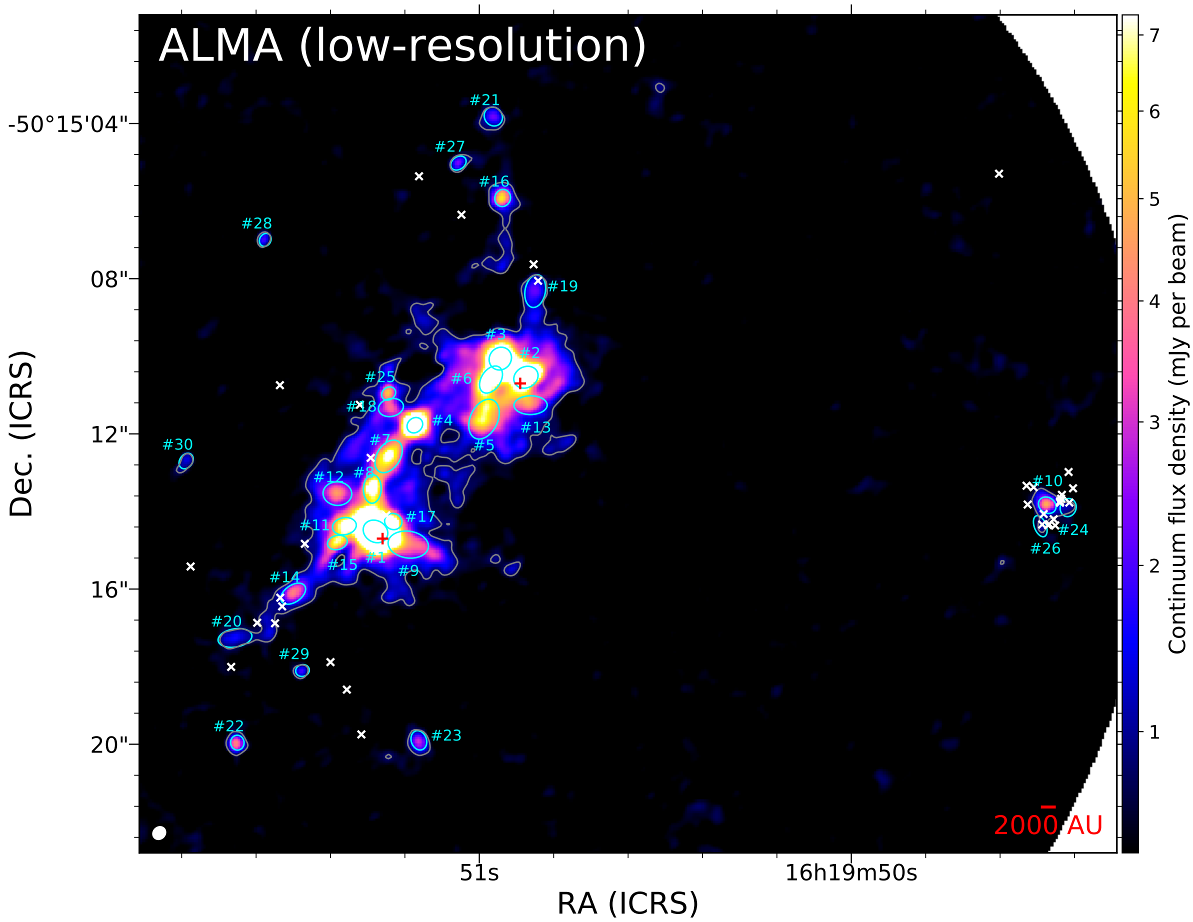

Extended Data Fig. 5 | ALMA low-resolution 1.3 mm continuum image. The green ellipses are dense cores identified from ALMA low-resolution 1.3 mm continuum image. The grey contours show the 7σ, where σ = 0.05 mJy beam^{-1}. The red plus and white cross symbols are Class II (ref. [23]) and Class I (ref. [50]) CH_3OH maser, respectively, indicating intense ongoing star formation activity. The synthesized beam size of 1.3 mm continuum image present in the lower left corner with a white ellipse.

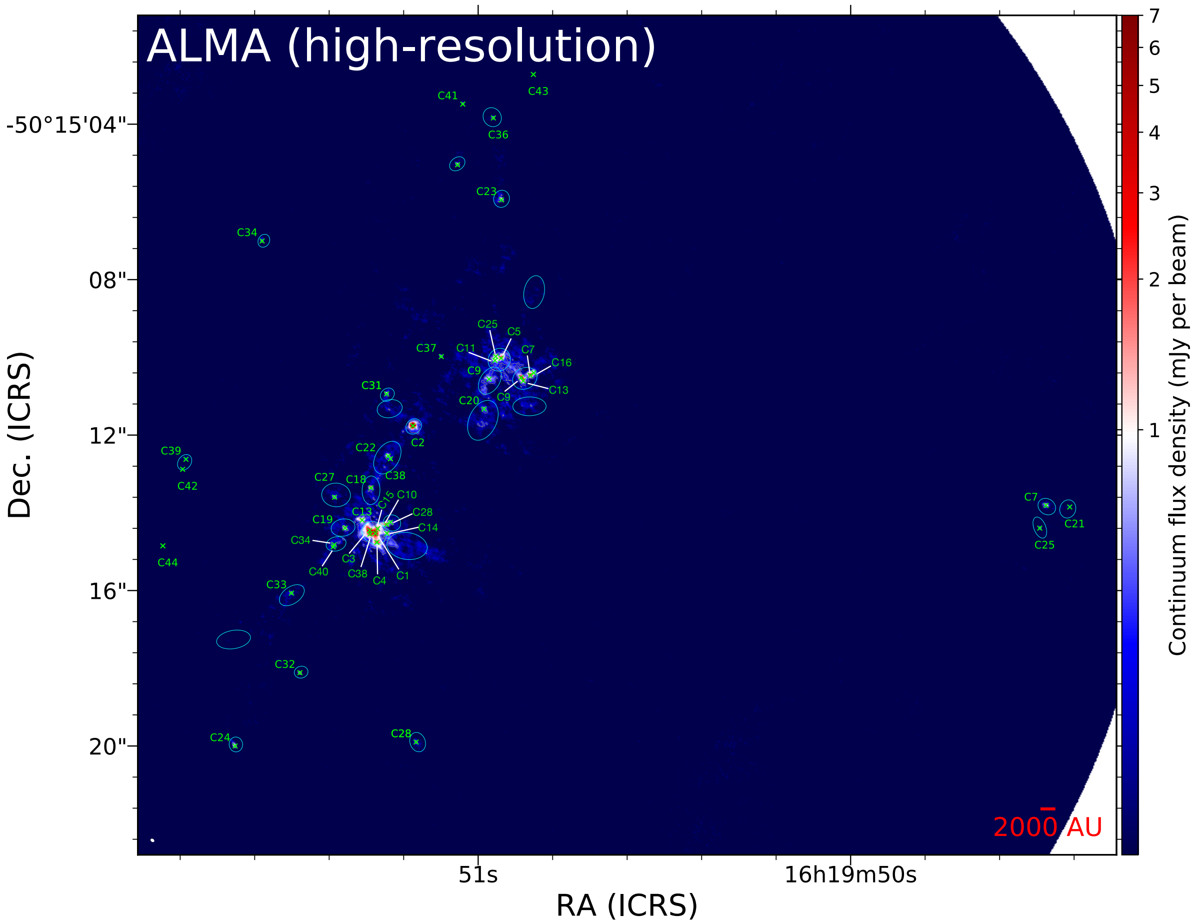

Extended Data Fig. 6 | ALMA high-resolution 1.3 mm continuum image. The cyan ellipses are the identified dense cores as shown in Extended Data Fig. 5. The green crosses show condensations identified from ALMA high-resolution 1.3 mm continuum image. The grey contours show the 7σ, where σ = 0.05 mJy beam^{-1}. The synthesized beam size of 1.3 mm continuum image present in the lower left corner with a white ellipse.

References

[1] Duchêne, Gaspard & Kraus, Adam, et al. *et al.* Stellar Multiplicity. *ARA&A* **51**, 269-310 (2013)

[2] Reipurth, B., et al. *et al.* Multiplicity in Early Stellar Evolution. *Protostars and Planets VI* , 267-290 (2014)

[3] Offner, Stella S. R., et al. *et al.* The Origin and Evolution of Multiple Star Systems. *arXiv e-prints* , arXiv:2203.10066 (2022)

[4] Lada, Charles J. & Lada, Elizabeth A., et al. *et al.* Embedded Clusters in Molecular Clouds. *ARA&A* **41**, 57-115 (2003)

[5] Zinnecker, Hans & Yorke, Harold W., et al. *et al.* Toward Understanding Massive Star Formation. *ARA&A* **45**, 481-563 (2007)

[6] Beltrán, M. T., et al. *et al.* Binary system and jet precession and expansion in G35.20-0.74N. *A&A* **593**, A49 (2016)

[7] Beuther, H., et al. *et al.* Multiplicity and disks within the high-mass core NGC 7538IRS1. Resolving cm line and continuum emission at $0.06'' \times 0.05''$ resolution. *A&A* **605**, A61 (2017)

[8] Zapata, Luis A., et al. *et al.* An Asymmetric Keplerian Disk Surrounding the O-type Protostar IRAS 16547-4247. *ApJ* **872**, 176 (2019)

[9] Zhang, Yichen. *et al.* Dynamics of a massive binary at birth. *Nature Astronomy* **3**, 517-523 (2019)

[10] Guzmán, Andrés E., et al. *et al.* A Photoionized Accretion Disk around a Young High-mass Star. *ApJ* **904**, 77 (2020)

[11] Tanaka, Kei E. I. *et al.* Salt, Hot Water, and Silicon Compounds Tracing Massive Twin Disks. *ApJ* **900**, L2 (2020)

[12] Olguin, Fernando A. *et al.* Digging into the Interior of Hot Cores with ALMA (DIHCA). II. Exploring the Inner Binary (Multiple) System Embedded in G335 MM1 ALMA1. *ApJ* **929**, 68 (2022)

[13] Offner, Stella S. R., et al. *et al.* The Formation of Low-mass Binary Star Systems Via Turbulent Fragmentation. *ApJ* **725**, 1485-1494 (2010)

[14] Kouwenhoven, M. B. N., et al. *et al.* The primordial binary population. II.. Recovering the binary population for intermediate mass stars in Scorpius OB2. *A&A* **474**, 77-104 (2007)

[15] Mason, Brian D. *et al.* The High Angular Resolution Multiplicity of Massive Stars. *AJ* **137**, 3358-3377 (2009)

[16] Sana, H. *et al.* Southern Massive Stars at High Angular Resolution: Observational Campaign and Companion Detection. *ApJS* **215**, 15 (2014)

[17] Portegies Zwart, Simon F., et al. *et al.* Young Massive Star Clusters. *ARA&A* **48**, 431-493 (2010)

[18] Sana H. *et al.* Binary Interaction Dominates the Evolution of Massive Stars. *Science* **337**, 444 (2012)

[19] Kratter, Kaitlin M., et al. *et al.* On the Role of Disks in the Formation of Stellar Systems: A Numerical Parameter Study of Rapid Accretion. *ApJ* **708**, 1585-1597 (2010)

[20] Pineda, Jaime E. *et al.* The formation of a quadruple star system with wide separation. *Nature* **518**, 213-215 (2015)

[21] Bate, Matthew R., et al. *et al.* The formation of a star cluster: predicting the properties of stars and brown dwarfs. *MNRAS* **339**, 577-599 (2003)

[22] Whitaker, J. Scott, et al. *et al.* MALT90 Kinematic Distances to Dense Molecular Clumps. *AJ* **154**, 140 (2017)

[23] Caswell, J. L. *et al.* The 6-GHz methanol multibeam maser catalogue - III. Galactic longitudes 330° to 345°. *MNRAS* **417**, 1964-1995 (2011)

[24] Kuruwita, Rajika L. & Haugbølle, Troels, et al. *et al.* The contribution of binary star formation via core fragmentation on protostellar multiplicity. *A&A* **674**, A196 (2023)

[25] Cournoyer-Cloutier, Claude, et al. *et al.* Implementing primordial binaries in simulations of star cluster formation with a hybrid MHD and direct N-body method. *MNRAS* **501**, 4464-4478 (2021)

[26] Lee, Aaron T., et al. *et al.* The Formation and Evolution of Wide-orbit Stellar Multiples In Magnetized Clouds. *ApJ* **887**, 232 (2019)

[27] Lu, Xing, et al. *et al.* A massive Keplerian protostellar disk with flyby-induced spirals in the Central Molecular Zone. *Nature Astronomy* **6**, 837-843 (2022)

[28] Panagia, N. Some Physical parameters of early-type stars. *AJ* **78**, 929–934 (1973).

[29] Eker, Z., et al. *et al.* Interrelated main-sequence mass-luminosity, mass-radius, and mass-effective temperature relations. *MNRAS* **479**, 5491-5511 (2018)

[30] Tobin, John J., et al. *et al.* The VLA/ALMA Nascent Disk And Multiplicity (VANDAM) Survey of Orion Protostars. V. A Characterization of Protostellar Multiplicity. *ApJ* **925**, 39 (2022)

[31] Foster, Jonathan B., et al. *et al.* The Millimeter Astronomy Legacy Team 90 GHz (MALT90) Pilot Survey. *ApJS* **197**, 25 (2011)

[32] Jackson, J. M., et al. *et al.* MALT90: The Millimetre Astronomy Legacy Team 90 GHz Survey. *PASA* **30**, e057 (2013)

[33] Hoq, Sadia, et al. *et al.* Chemical Evolution in High-mass Star-forming Regions: Results from the MALT90 Survey. *ApJ* **777**, 157 (2013)

[34] Stephens, Ian W. *et al.* Interferometric Observations of High-Mass Star-Forming Clumps With Unusual N_2H^+/HCO^+ Line Ratios. *ApJ* **802**, 6 (2015)

[35] Menten, Karl M. *et al.* The Discovery of a New, Very Strong, and Widespread Interstellar Methanol Maser Line. *ApJ* **380**, L75 (1991)

[36] Breen, S. L. *et al.* Confirmation of the exclusive association between 6.7-GHz methanol masers and high-mass star formation regions. *MNRAS* **435**, 524-530 (2013)

[37] Olguin Olguin, Fernando A., et al. *et al.* Digging into the Interior of Hot Cores with ALMA (DIHCA). I. Dissecting the High-mass Star-forming Core G335.579-0.292 MM1. *ApJ* **909**, 199 (2021)

[38] Taniguchi, Kotomi, et al. *et al.* Digging into the Interior of Hot Cores with the ALMA (DIHCA). III. The Chemical Link between NH¡SUB¿2¡/SUB¿CHO, HNCO, and H¡SUB¿2¡/SUB¿CO. *ApJ* **950**, 57 (2023)

[39] McMullin, J. P. *et al.* CASA Architecture and Applications. *Astronomical Data Analysis Software and Systems XVI* **376**, 127 (2007)

[40] Contreras, Yanett. *et al.* Infall Signatures in a Prestellar Core Embedded in the High-mass 70 μm Dark IRDC G331.372-00.116. *ApJ* **861**, 14 (2018)

[41] Rosolowsky, E. W., et al. *et al.* Structural Analysis of Molecular Clouds: Dendrograms. *ApJ* **679**, 1338-1351 (2008)

[42] Beltrán, M. T. & de Wit, W. J., et al. *et al.* Accretion disks in luminous young stellar objects. *A&A Rev.* **24**, 6 (2016)

[43] Möller, T., et al. *et al.* eXtended CASA Line Analysis Software Suite (XCLASS). *A&A* **598**, A7 (2017)

[44] Scoville, N. Z. & Kwan, J. Infrared sources in molecular clouds. *ApJ* **206**, 718–727 (1976).

[45] Garay, G. & Lizano, S. Massive Stars: Their Environment and Formation. *PASP* **111**, 1049–1087 (1999).

[46] Goldsmith, Paul F. *et al.* Molecular Depletion and Thermal Balance in Dark Cloud Cores. *ApJ* **557**, 736-746 (2001)

[47] Urquhart, J. S., et al. *et al.* ATLASGAL - properties of a complete sample of Galactic clumps. *MNRAS* **473**, 1059-1102 (2018)

[48] Frau, P., et al. *et al.* Young Starless Cores Embedded in the Magnetically Dominated Pipe Nebula. *ApJ* **723**, 1665-1677 (2010)

[49] Ossenkopf, V. & Henning, T. Dust opacities for protostellar cores. *A&A* **291**, 943–959 (1994).

[50] Voronkov, M. A. *et al.* Southern class I methanol masers at 36 and 44 GHz. *MNRAS* **439**, 2584-2617 (2014)